Nano Energy 66 (2019) 104088

Contents lists available at ScienceDirect

Nano Energy

journal homepage: www.elsevier.com/locate/nanoen

Full paper

# High loading single-atom Cu dispersed on graphene for efficient oxygen reduction reaction

Guokang Han[a], Yu Zheng[a], Xue Zhang[b], Zhiqiang Wang[c], Yue Gong[d], Chunyu Du[a,**], Mohammad Norouzi Banis[e], Yun-Mui Yiu[c], Tsun-Kong Sham[c], Lin Gu[d], Yongrong Sun[a], Yajing Wang[a], Jinpeng Wang[a], Yunzhi Gao[a], Geping Yin[a], Xueliang Sun[e,*]

[a] School of Chemistry and Chemical Engineering, Harbin Institute of Technology, Harbin, 150001, China
[b] Shenzhen Institute of Advanced Technology, Chinese Academy of Sciences, Shenzhen, 518048, China
[c] Department of Chemistry, University of Western Ontario, London, Ontario, N6A 5B9, Canada
[d] Institute of Physics, Chinese Academy of Sciences, Beijing, 100190, China
[e] Department of Mechanical and Materials Engineering, University of Western Ontario, London, Ontario, N6A 5B9, Canada

ARTICLE INFO

*Keywords:*
Single-atom Cu dispersed on graphene
Confined self-initiated protocol
High loading level
Electrocatalysis
Oxygen reduction reaction

ABSTRACT

Single-atom metal dispersed on graphene materials are highly desired in various fields such as energy conversion/storage, catalysis and nanoelectronics. However, the fabrication of such materials with high loading level is still challenging, as the conventional pyrolysis protocol usually leads to metal agglomeration due to the poor thermal stability of metal precursors and the high surface energy of single-atom metals. Herein, we demonstrate the fabrication of single-atom Cu dispersed on graphene (Cu/G) with ultrahigh Cu loading of 5.4 wt%, using a unique confined self-initiated dispersing protocol. It is revealed that Cu is introduced into graphene matrix via highly active gaseous Cu-containing intermediate, which results in abundant and well-dispersed Cu-containing moieties. This Cu/G material with ultrahigh loading level as an electrocatalyst presents remarkable activity towards the oxygen reduction reaction (ORR) due to the abundant and highly dispersive Cu single atoms, even outperforming the commercial Pt/C. Our findings not only facilitate the development of single-atom metal dispersed on graphene materials but also highlight the importance of tuning active site structures in non-noble metal electrocatalysis.

## 1. Introduction

Recent years have witnessed the boosting research on metal single-atom materials because of their 100% metal dispersion and tunable electronic structures highly distinctive from the bulk counterparts [1–3]. These unique features make the metal single-atom materials attractive in various fields such as energy conversion/storage, sensing, catalysis and nanoelectronics [4–8]. In particular, single-atom catalysis has become the most active and promising frontier. The single-atom catalysts (SACs) with largely tuned catalytic activity/selectivity have been explored to various chemical, [9–13] electrochemical, [14–16] and photochemical reactions [17]. The dispersing substrate is proved to be vital to metal SACs. Graphene with $sp^2$-hybridized carbon structure is an ideal substrate for dispersing metal SACs, due to its superior electrical conductivity, large specific surface area, exceptional mechanical strength and high flexibility [18–20]. Graphene-based SACs have exhibited excellent catalytic properties in organic reactions, [21,22] $CO_2$ reduction, [23,24] and $H_2$ evolution [25–30].

Unfortunately, the loading of metal SACs on graphene, and other substrates as well, is usually rather low due to the aggregation tendency of metal atoms, which is a major barrier to the application of metal SACs [21,31–33]. The most conventional method for the fabrication of graphene-based SACs is the high-temperature pyrolysis of graphene oxide and metal salts. For instance, single atom Ni on graphene was obtained by the high-temperature treatment of the mixture of graphene oxide, dicyandiamide and nickel nitrate, [4] while Co and Fe were atomically dispersed on graphene by the pyrolysis of graphene oxide and corresponding metal chlorides in ammonia atmosphere [6,27,34]. However, single-atom metals are thermodynamically unstable due to their high surface energy and tend to agglomerate into clusters or even nanoparticles during the pyrolysis process (Fig. 1 upper diagram). To tackle this issue, only limited amount of metal salt can be introduced in

* Corresponding author.
** Corresponding author.
*E-mail addresses:* cydu@hit.edu.cn (C. Du), xsun9@uwo.ca (X. Sun).

https://doi.org/10.1016/j.nanoen.2019.104088
Received 17 July 2019; Received in revised form 20 August 2019; Accepted 2 September 2019
Available online 03 September 2019
2211-2855/ 

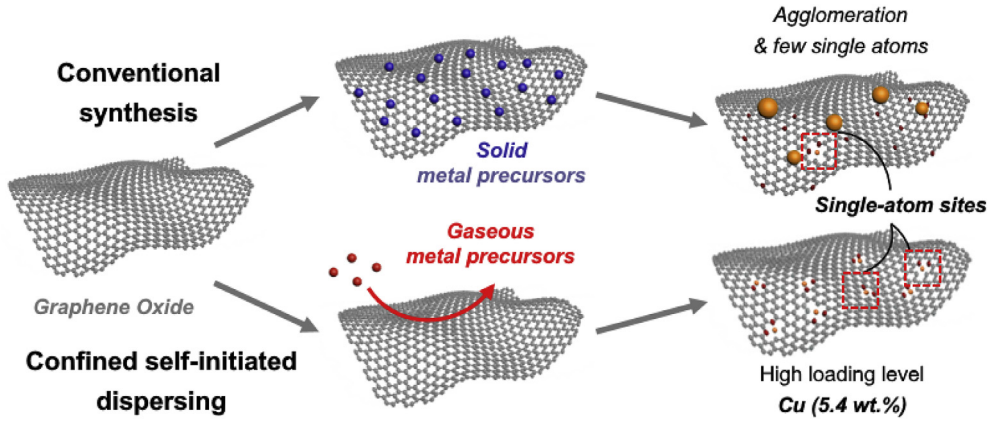


**Fig. 1.** Schematic illustration of (upper) conventional and (lower) confined self-initiated dispersing protocols for the synthesis of metals dispersed on graphene.

the precursors. Therefore, the loading level of single-atom metals on graphene is barely satisfactory (Table S1, Supporting Information), and high loading dispersion of metal single atom is still quite challenging.

Herein, we report single-atom Cu dispersed on graphene with high loading level via a unique confined self-initiated dispersing protocol, simply by pyrolysis of graphene oxide (GO) and dicyandiamide (DICY) in a copper container (Fig. 1 lower diagram, see Experimental Section for details). During the pyrolysis, DICY first decomposes into highly reactive nitrogen-containing gas, which further reacts with copper container to in-situ generate Cu-containing gaseous precursor. This precursor is rather active at high-temperature, inducing abundant and well-dispersed Cu single atoms on the graphene matrix. The innovative dispersing process avoids the massive agglomeration of metal atoms in the conventional procedures, and the loading level of single-atom Cu reaches up to 5.4 wt%, the highest value in single metal atoms dispersed on graphene reported so far. This Cu/G with high loading level as an electrocatalyst presents remarkable activity towards the oxygen reduction reaction (ORR), even outperforming the commercial Pt/C catalyst.

## 2. Experimental Section

### 2.1. Material synthesis

Cu/G: Graphene oxide (GO) was synthetized according to the previously reported work [34]. Typically, 240 mg dicyandiamide (DICY) was added into 20 mL graphene oxide dispersion (1 mg $mL^{-1}$) and stirred for 10 h, which was freeze-dried to obtain the GO/DICY mixture. The mixture was added into a quartz boat, which was partially covered by a quartz plate to prevent the samples from contaminating. The entire quartz boat was tightly wrapped with a piece of Cu foil, and pyrolysed at 600 °C for 2 h and 800 °C for 1 h under flowing Ar in a tube furnace. The product was treated in $O_2$ saturated 0.5 mol $L^{-1}$ $H_2SO_4$ solution at 80 °C for 10 h to remove the impurities. After thoroughly washing with deionized water, the product underwent a second pyrolysis at 300 °C under Ar to obtain the final Cu/G. For comparison, pristine graphene (p-G) and N-doped graphene (N-G) samples were synthesized in the same procedure as Cu/G, except that GO alone was used as precursor and a normal quartz boat without Cu foil was utilized, respectively.

### 2.2. Physical characterization

The morphology of the samples was investigated by transmission electron microscopy (TEM) using a JEOL JEM2010 TEM with 200 kV accelerating voltage, and high-angle annular dark-field scanning transmission electron microscopy (HAADF-STEM) using a probe aberration corrected microscope, JEOL JEM-ARM200CF, equipped with cold field emission gun, operated at 200 kV. Energy dispersive X-ray spectroscopy (EDS) was recorded with a SDD-type detector. The attainable energy resolution of the detector is 130 eV. The crystal structure was analyzed using X-ray diffraction (XRD) performed on a Rigaku D/max-rB diffractometer with Cu Kα (λ = 1.5406 Å) radiation at step size of 0.026°. The specific surface area and pore structure were determined by a Beishide 3H-2000PS2 BET surface area analyzer. The chemical composition was studied by X-ray photoelectron spectroscopy (XPS) performed on a Physical Electronics PHI model 5700 instrument using Al Kα radiation. The binding energy for all samples was corrected by the C1s peak of advantageous carbon at 284.6 eV. The mass fraction of Cu in samples was detected by inductively coupled plasma optical emission spectrometry (ICP-OES), performed on PerkinElmer Optima 5300DV ICP-OES System. Fourier transform infrared spectroscopy (FTIR) was conducted on a Thermo Scientific Nicolet iS10 FT-IR spectrometer. Raman spectroscopy were recorded on a JY HR800 Raman spectrometer using 457.9 nm laser. Thermogravimetric analysis-mass spectrometry (TG-MS) was conducted on Netzsch STAA449C16/G + QMS403 in Ar atmosphere. Detailed chemical structure of samples was investigated by Cu K-edge X-ray absorption near edge structure (XANES) and extended X-ray absorption fine structure (EXAFS) measurements, conducted at the HXMA beamline of the Canadian Light Source.

### 2.3. Electrochemical measurements

Typically, 2.6 mg catalyst powder was added into 30 μL Nafion (5 wt %, DuPont) and 520 μL mixture of water (18.25 MΩ cm, Milli-Q) and isopropanol (ACS grade, Aladdin Reagent) in 3:1 volume to form a homogenous ink assisted by ultrasound. Certain amount of catalyst ink was pipetted onto a polished glassy carbon rotating disk electrode (RDE, 3 mm in diameter) or disk of rotating ring-disk electrode (RRDE, 5.6 mm in diameter) to obtain the catalyst loading of 0.4 mg $cm_{disk}^{-2}$. For Pt/C (20 wt%, Alfa Aesar), a catalyst loading of 0.1 mg $cm_{disk}^{-2}$ was adopted. A three-electrode cell was used for the electrochemical measurements. Before using, the three-electrode glass cell was soaked in saturated sulfuric acid and rinsed multiple times with ultrapure Milli-Q water. The catalyst-coated RDE (or RRDE) connected to a PINE 636 RDE system was used as the working electrode. An Hg/HgO electrode and a Pt foil (1 cm × 1 cm) were used as the reference and counter electrodes, respectively. All the electrochemical measurements except chronoamperometry were conducted using a CHI 720b electrochemical workstation at 25 °C. For each electrochemical measurement, 50 mL freshly prepared 0.1 mol $L^{-1}$ KOH (99.999% metal basis, Aladdin Reagent) aqueous solution was used as the electrolyte. The reference electrode was calibrated by a Pt foil immersed in $H_2$ (99.999%) saturated KOH solution. All the electrode potentials in this work were referenced to the reversible hydrogen electrode (RHE).

The ORR polarization curves were recorded in $O_2$ (99.999%)

saturated KOH solution at a scanning rate of 10 mV $s^{-1}$ between 1.0 V and 0.0 V at different rotating rates. The potential of ring disk was kept at 1.2 V in RRDE tests. The chronoamperometry tests were carried out at 0.65 V in $O_2$ saturated KOH using a CHI 6081 electrochemical workstation. Accelerated durability tests (ADTs) were conducted by performing potential scan between 0.6 V and 1.0 V for 10000 cycles at a scanning rate of 100 mV $s^{-1}$ in $O_2$ (99.999%) saturated KOH.

Kinetic current density ($i_k$) of catalysts was calculated by the Koutecky-Levich equation [35]:

$$\frac{1}{i} = \frac{1}{i_k} + \frac{1}{i_d} = \frac{1}{i_k} - \frac{1}{B\varpi^{1/2}}$$

where $i$, $i_k$ and $i_d$ represent apparent current density, kinetic current density and diffusion-limited current density (mA $cm^{-2}$), respectively; ω is the rotating rate of the electrode (rpm); $B$ is a coefficient depending on the properties of electrolyte.

Turnover frequency (TOF) was calculated by the following equation [36]:

$$TOF = \frac{i_k M_{metal}}{c_{cat.}\varpi_{metal} F}$$

where $M_{metal}$ is the molar mass of metal element, $c_{cat.}$ is the mass loading of catalyst on the electrode (0.4 mg $cm^{-2}$ for Cu/G or 0.1 mg $cm^{-2}$ for Pt/C), $\omega_{metal}$ represents the mass ratio of metal in catalyst (5.4% for Cu/G and 20% for Pt/C), and $F$ is Faraday constant (96485 C $mol^{-1}$).

Electron transfer number ($n$) and $HO_2^-$ yield ($HO_2^-$%) were calculated by the following equations [37]:

$$n = \frac{4I_d}{I_r/N + I_d}$$

$$HO_2^-\% = \frac{200I_r/N}{I_r/N + I_d}$$

where $I_d$ and $I_r$ were disk current and ring current, respectively, and $N$ is the ring current collection efficiency (0.37).

### 2.4. Zn-air battery assembly and testing

The electrochemical tests of Zn-air batteries were conducted using home-made coin cells (CR2025 type), consisting of an air cathode, a polished Zn plate anode, a glass filter separator (Whatman) and 6.0 mol $L^{-1}$ KOH solution as electrolyte. The mixture of XC-72r carbon black and polytetrafluoroethylene (60 wt%, DuPont) was roll-pressed onto a nickel foam to form the gas diffusion layer. The air electrode was fabricated by pipetting certain amount of catalyst ink onto the gas diffusion layer with a catalyst loading of 0.4 mg $cm^{-2}$ for both Cu/G and Pt/C. The Zn-air battery polarization curves were collected on a CHI 6081 electrochemical workstation at 25 °C in ambient air using galvanodynamic method at a scan rate of 1 mA $s^{-1}$.

### 2.5. Computation methods

The density functional theory (DFT) calculations for ORR on Cu (111) and $CuN_2$ adopted graphene supercell were performed by using freely available CP2K/Quickstep package [38]. Cu(111) was modeled by a four-layer slab of p(4 × 4) super-cell and the size of simulation box was 10.224 × 10.224 × 21.261 $Å^3$. Neighboring slabs were separated by a vacuum of 15 Å to avoid spurious self-interactions. Monkhorst-Pack k-point meshes of 4 × 4 × 1 were used for these periodic models. An energy cutoff of 400 eV was employed for the plane-wave basis set. The convergence threshold for ionic steps in geometry optimization was $1 \times 10^{-4}$ eV. Geometries were deemed converged when the forces on each atom were below 0.02 eV $Å^{-1}$. A frequency analysis was carried out on the stable states in order to confirm that these represented genuine minima. All of the electronic energies were corrected for zero-point energy (ZPE) contributions. For $CuN_2$ adopted graphene supercell, the 2s, 2p electrons of the O, C and N atoms and the 4s, 3d electrons of the Cu atoms were treated as valence electrons. We used Perdew-Burke-Ernzerhof (PBE) functional with Grimme's dispersion correction [39]. The core electrons were represented by analytic Goedecker-Teter-Hutter (GTH) pseudopotentials [40,41]. The Gaussian basis sets were double-ζ with one set of polarization functions (DZVP) [42]. The plane wave cutoff for the electron density was 400 Ry.

To explore the free energy profile along the ORR pathway, the change in Gibbs free energy for all intermediates has been evaluated using the following relation:

$$\Delta G = \Delta E - T\Delta S - neU$$

where E is the total energy calculated from DFT. S, entropy, can be obtained directly from a physical chemistry table [43]. The n represents the number of transferred electrons, e is the elementary charge and U is the operating electrochemical potential in standard hydrogen electrode (SHE).

In order to calculate the change in S of the molecules, $O_2$, $H_2$ and $H_2O$ molecules are considered to be in gas phase at room temperature and under ambient pressure. It is also considered that the entropy of the adsorbed states of the molecules are negligible compared to that in their gas phase. The free energies of $H_2O$(l), $O_2$ (g) and $OH^-$ are estimated from the following equations:

$$G_{H_2O(l)} = G_{H_2O(g)} + RT\ln(\frac{p}{p_0})$$

$$G_{O_2(g)} = 2G_{H_2O(l)} - 2G_{H_2(g)} + 4.92\text{eV}$$

$$G_{OH^-} = G_{H_2O(l)} - G_{H^+} = G_{H_2O(l)} - \frac{1}{2}G_{H_2(g)} + k_B T \ln 10 \times pH$$

where R is the gas constant, T = 298.15 K, $p$ = 0.035 bar and $p_0$ = 1 bar. As indicated earlier, in this free energy analysis, "$H^+ + e^-$" has been assumed to be in equilibrium with 1/2 $H_2$, at pH = 0 and 0 V potential in SHE.

## 3. Results and discussion

### 3.1. Physical characterization

The morphology of the as-prepared Cu/G sample is characterized by transmission electron microscopy (TEM). Fig. 2a identifies the large and semitransparent microsheets with many wrinkles, a typical graphene morphology (Fig. S1 in Supporting Information), [44,45] indicating that the confined self-initiated dispersing process causes negligible morphology damage. The lattice fringe is measured to be ~0.34 nm from the wrinkles in the high resolution TEM image (Fig. 2b), which is in good agreement with the (002) crystalline plane of graphene and reveals the reduction of GO to graphene during the pyrolysis process. Meanwhile, the selected area electron diffraction (SAED) pattern verifies the presence of graphene without any highly-crystallized phases (inset in Fig. 2b) [46]. Moreover, the uniform distribution of Cu signals in the energy dispersive spectroscopy (EDS) elemental mappings (Fig. 2c) suggests the substantial dispersion of atomic Cu on the graphene matrix. Further characterization using spherical aberration corrected HAAFD-STEM reveals a significant number of bright dots on a graphene sheet (highlighted in Fig. 2d). These dots can be identified as single-atom Cu because the Z-contrast of Cu is much different from that of lighter elements such as C, N or O [27,47,48]. The number density of single Cu atoms in Fig. 2d is roughly estimated to be ca. 2 $nm^{-2}$. The loading level of single-atom Cu in our Cu/G material is detected by ICP-OES to reach up to 5.4 wt%. To the best of our knowledge, this is the highest single-atom metal loading level on graphene ever reported (Table S1), which should be ascribed to the unique confined self-initiated dispersing protocol.

The XRD pattern of Cu/G material (Fig. S2) shows a broad peak at

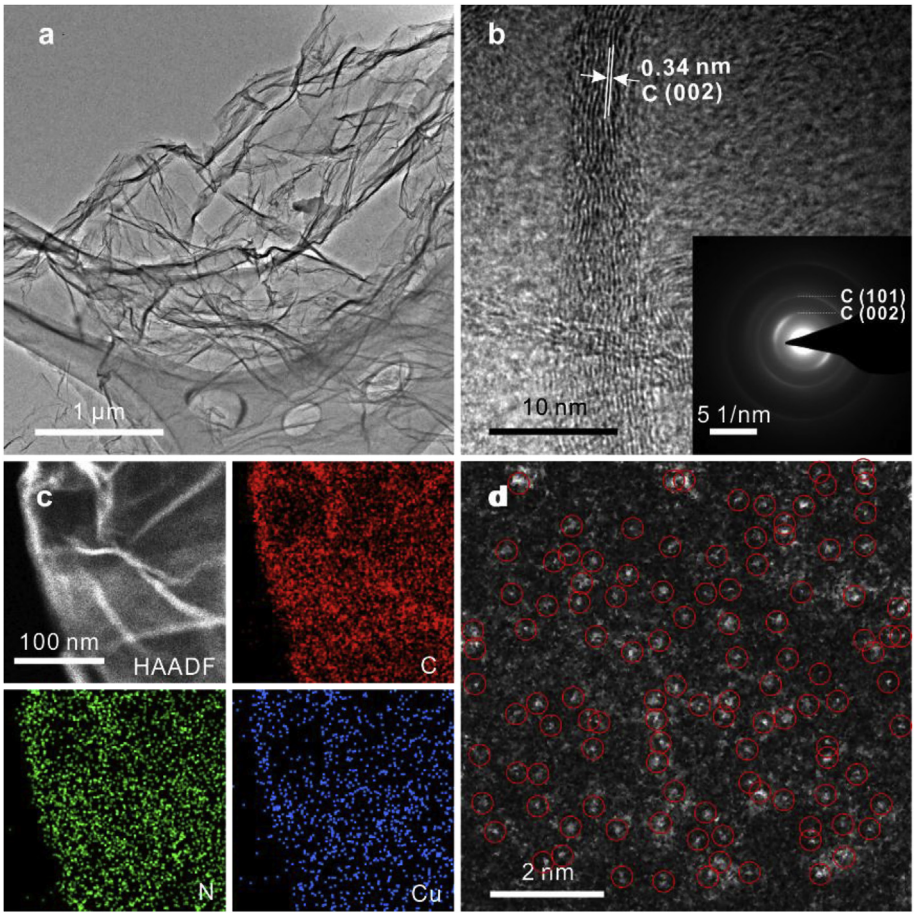


**Fig. 2. Microscopic characterization of Cu/G.** (a) TEM image of Cu/G; (b) HRTEM image of a wrinkle and (inset) SEAD pattern of Cu/G; (c) STEM-EDS elemental mappings of C, N and Cu; (d) spherical aberration corrected HAADF-STEM image of Cu/G showing the presence of single atom Cu.

26.7° corresponding to the (002) plane of graphitic carbon, [49] which is in consistence with the lattice fringe and SEAD pattern in Fig. 2b. Moreover, the pattern of Cu/G shares the same characteristics to that of pristine graphene (p-G) prepared by the similar procedure (see Experimental Section), revealing their alike crystal structure. The XRD pattern of Cu/G does not show any diffraction peak from copper and its oxides/carbides/nitrides, which suggests that there are no impurity present in Cu/G. The carbonous structure of Cu/G is revealed by Raman spectroscopy (Fig. 3a). The distinct G band (1577 $cm^{-1}$) and D band (1357 $cm^{-1}$) represent the graphitic and disordered carbon, respectively [50]. The higher intensity ratio of D and G bands for Cu/G (1.07) than that for p-G (0.83) proves a greater amount of defects in Cu/G matrix, [51] which should result from for the Cu atom dispersion.

The surface chemical environment of Cu/G is analyzed by XPS. In high resolution Cu 2p spectrum (Fig. 3b), the major peaks centered at 932.0 eV and 952.0 eV correspond to the metallic/monovalent Cu (those at 934.3 eV and 954.3 eV are from divalent Cu due to oxidation) [52,53]. Because the binding energies of Cu(0) and Cu(I) are too close to be separated in Cu 2p XPS spectrum, LMM Auger spectrum is characterized (inset in Fig. 3b). Both the peak centered at 916.3 eV and the Auger parameter of 1848.7 eV demonstrate the richness of Cu(I) in Cu/G, [54] which will be further confirmed by XANES result. The dispersion of single-atom Cu onto graphene is further supported by the high atomic ratio of pyridinic N (55.2 at.% of total N, Fig. S3a), which is believed to be the anchor sites for single-atom metal through coordination.

XANES and EXAFS are conducted to probe the local electronic structure of Cu in Cu/G. The white line of Cu K-edge for Cu/G shifts towards higher energy compared with metallic Cu to a position between $Cu_2O$ and CuO (Fig. 3c), revealing a positive oxidation state of Cu in Cu/G [55,56]. Further, the first derivative of XANES curve for Cu/G (Fig. 3d) presents a distinct peak closest to $Cu_2O$, clearly confirming the cuprous nature of Cu in Cu/G, in agreement with the XPS analysis. Since the presence of crystallized cuprous species have already been ruled out by TEM and XRD, Cu(I) should be ascribed to single-atom Cu, whose oxidation state results from the partial electron transfer to its coordinated atoms [57]. This transfer is confirmed by the calculated charge density difference of a single Cu atom coordinated with N atoms in graphene matrix shown in Fig. S3b. As shown in the Fourier transformed EXAFS (Fig. 3e) without phase correction, the main peak of Cu/G centers at 1.5 Å in the R space, which should correspond to the Cu-N bond [24,58]. Meanwhile, neither obvious peaks assigned to the Cu-Cu coordination at 2.2 Å as in the case of metallic Cu nor Cu-O at 1.4 Å in $Cu_2O$ can be observed, demonstrating that the Cu atoms are atomically dispersed, in accordance with the HAADF-STEM observation.

In order to further uncover the coordination environment of single-atom Cu, the EXAFS spectroscopy measured with FLY (Fluorescence Yield) mode is numerically fitted by the real space multiple scattering program of FEFF9, [59] and the result is shown in Fig. 3f. It is revealed that Cu in our Cu/G material is coordinated with 2 nitrogen atoms in form of Cu(I)-$N_2$ coordination. This local structure is different from commonly reported Fe-$N_4$ and Co-$N_4$ coordination, [60] providing an alternative site environment for chemical applications.

### 3.2. Dispersing mechanism of single Cu atom

Controlled experiments are carried out to clarify the confined self-initiated dispersing process. Pyrolysis temperature is found to be a vital

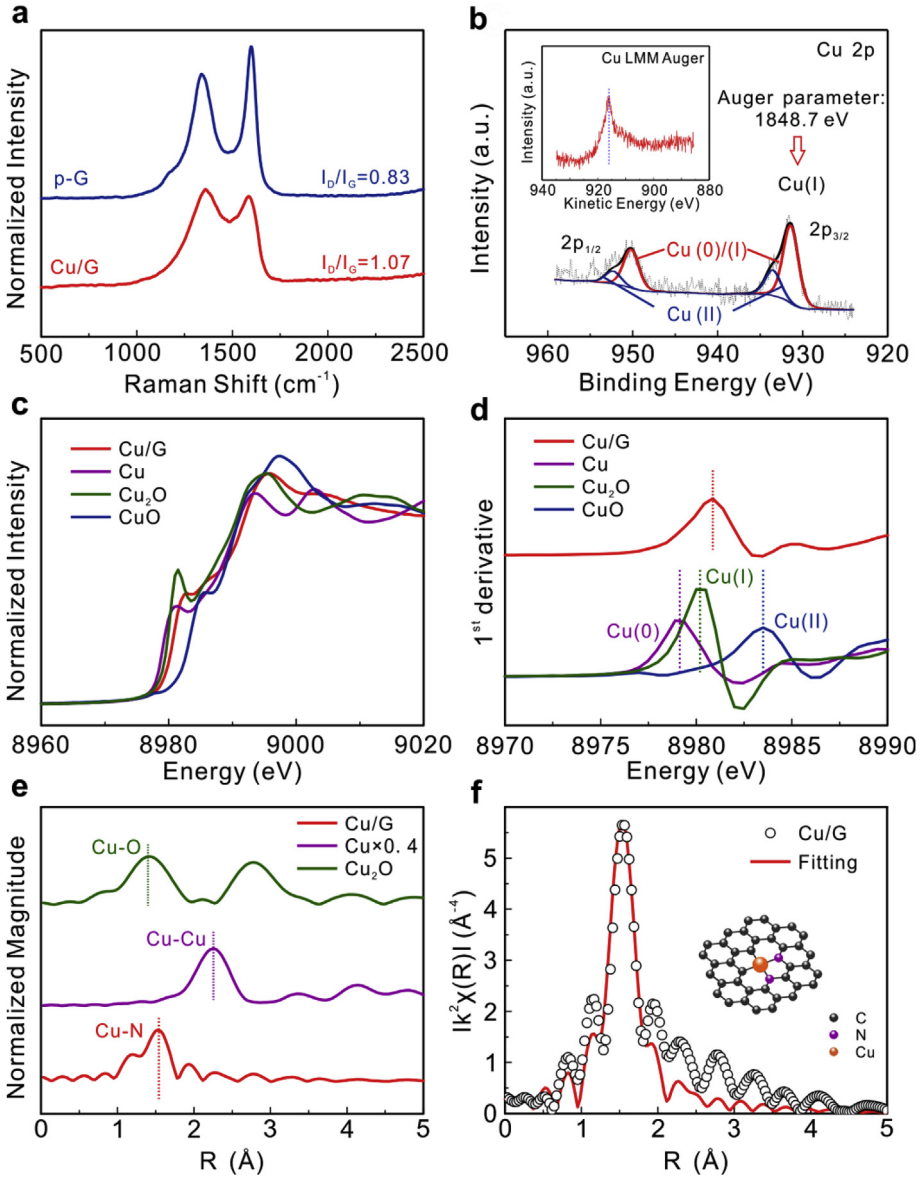


**Fig. 3. Investigation on the detailed structure of Cu/G.** (a) Raman spectra of p-G and Cu/G; (b) high-resolution XPS spectra of Cu 2p and (inset) Cu LMM Auger of Cu/G; (c) normalized Cu K-edge XANES spectra, (d) first derivatives of XANES and (e) Fourier transform of EXAFS for Cu/G and references; (f) EXAFS R space fitting curves of Cu/G and (inset) schematic illustration of best-fitted structure.

factor. As suggested by thermogravimetric (TG) curve (Fig. 4a), the mixture of DICY and GO gradually loses weight from 200 °C to 600 °C, and experiences a sharp weight loss from 600 °C to 730 °C, which should be attributed to the decomposition of DICY because of the similar thermal behavior between the mixture and pure DICY (Fig. S4).

The products pyrolyzed at different temperatures (denoted as Cu/G-T, where T represents temperature) are characterized by FTIR and XPS to help understand the confined self-initiated dispersing process. In FTIR spectra (Fig. 4b), a series of peaks assigned to the vibration of C-N heterocycles at 1200 $cm^{-1}$, 600 $cm^{-1}$ and a characteristic peak indexed to the triazine unit in $C_3N_4$ at 809 $cm^{-1}$ are observed [61]. Since the peak of triazine unit is only observed for Cu/G-600 but vanishes for Cu/G-700, it can be confirmed that $C_3N_4$ is produced during the first stage of pyrolysis below 600 °C and completely decomposes above 700 °C, consistent with the TG analysis (Fig. S4) and literature [62,63]. Notably, the signal of Cu is detected only for Cu/G-700 in the XPS spectra (Fig. 4c), indicating that the introduction of Cu is closely related to the decomposition of $C_3N_4$ in the second stage of pyrolysis. Further, it is found that if pyrolyzing GO alone in Cu container, no Cu is detected and by altering the mass ratio of DICY to GO ($m_{DICY}/m_{GO}$) in precursor, an apparent positive correlation between Cu content and $m_{DICY}/m_{GO}$ can be observed (Fig. 4d). At the same time, when using a quartz alone without Cu, much lower N fraction is observed in graphene (6.1 at.% compared with 10.1 at.% for Cu/G), suggesting that there is an apparent synergy between Cu and N.

The gaseous products in the thermal decomposition process of GO/DICY are analyzed using thermal gravimetric-mass spectrometry (TG-MS) as shown in Fig. S5 in Supporting Information. During the first stage of pyrolysis from ~200 °C to ~600 °C, a series of peaks with various mass-to-charge ratios ($m/z$) are detected. The signal of $m/z = 17$ assigned to $NH_3$ marks the decomposition of DICY and its polymerization to $C_3N_4$ [63–65]. In the second stage of weight loss (> 600 °C), a dramatic rise of the signal at $m/z = 30$ (assigned to $CH_3NH_2$ or $NH_2NH_2$) can be clearly observed along with the decomposition of $C_3N_4$ [62]. In the presence of Cu, however, the signal of $m/z = 30$ completely vanishes (Fig. 4a), indicating that these decomposition products is related to the generation of Cu-containing gaseous intermediates responsible for the confined self-initiated dispersing.

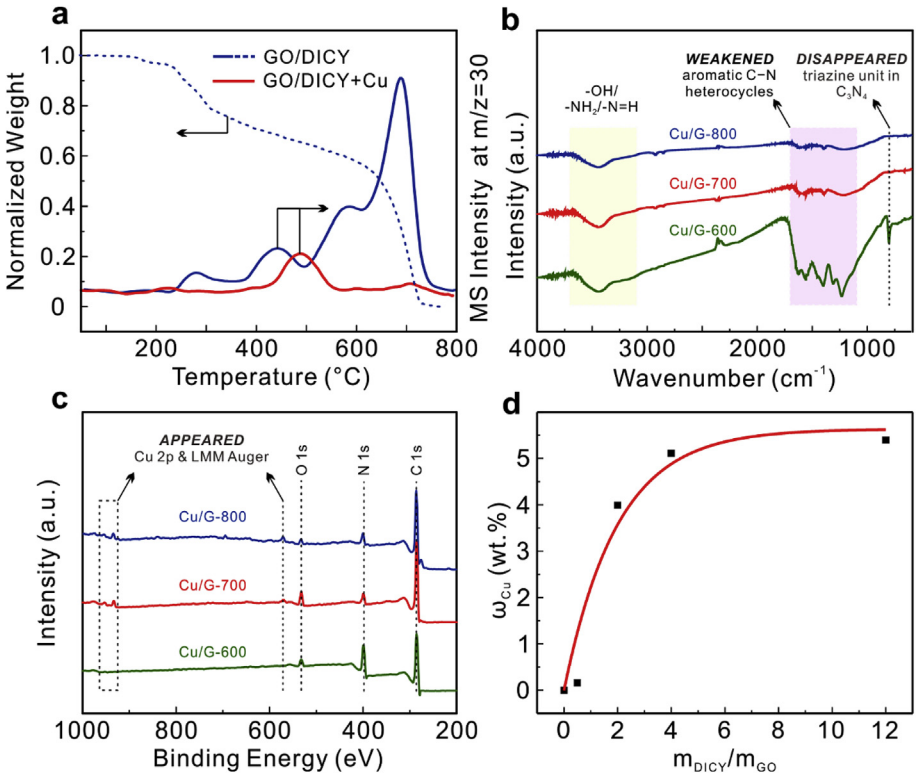


**Fig. 4. Investigation on the formation mechanism of Cu/G via confined self-initiated dispersing protocol.** (a) TG-MS signals of GO/DICY and MS signal of GO/DICY + Cu; (b) FTIR and (c) XPS spectra for Cu/G pyrolyzed at different temperatures; (d) atomic ratio of Cu in the resultant material as a function of mass ratio of DICY to GO in precursor.

According to the results of controlled experiment simulating the reaction procedure (illustrated in Fig. S6) by feeding methylamine or hydrazine carried by Ar into the heated furnace with Cu foil and GO placed sequentially, it is most likely that methylamine or hydrazine detected by TG-MS are the products derived from highly active reactants (radicals or instable molecules), rather than the direct reactants themselves, as the simulation experiments failed to introduce Cu into graphene.

When detecting the Cu-containing intermediates using TG-MS conducted on GO/DICY + Cu, however, no such chemicals were able to be detected. The most reasonable explanation would be the high activity and short life of Cu-containing intermediate, which may transfer into more stable species during their way out of TG through an adapter with much lower temperature (300 °C) to be detected by MS. These evidences lead us to believe that the high loading of Cu is achieved via the highly active and short-lived reactants Cu-containing intermediates, which are in-situ generated from the reaction between Cu and the decomposition products of $C_3N_4$ during high temperature pyrolysis. These highly active intermediates can partially break the graphene structure and disperse Cu on graphene, which is well evidenced by the higher intensity ratio of D and G bands in Raman spectrum for Cu/G.

### 3.3. Electrocatalysis towards ORR

Single-atom metal dispersed on carbon as active sites have shown promising activities towards a wide range of chemical and electrochemical reactions, including the oxygen reduction reaction (ORR), [27,66,67] which is the limiting half-reaction for fuel cells and metal-air batteries. At present, single-atom Fe dispersed on carbon are usually investigated as the non-precious metal (NPM) ORR catalysts because of their higher ORR activity. However, the nature of Fe species facilely catalyzes the decomposition of $H_2O_2$, an unwanted but inevitable product of ORR, into oxygen-containing radicals, which is known as the Fenton reaction [68–70]. These highly active radicals can attack the catalyst itself and other key materials in fuel cells or metal-air batteries, leading to their substantial performance degradation [71]. Thus, the exploration of other NPM ORR catalysts is of great interest in terms of practical applications.

Since Cu is less active in Fenton reaction, and Cu-based centers in biological system like cytochrome c oxidase and laccase can catalyze ORR efficiently, [53] we assess the ORR activity of our Cu/G with high loading level. To quantify the ORR activity, the polarization curves are measured by the rotating disk electrode (RDE) approach. The Cu/G samples as ORR catalyst are optimized at different pyrolysis temperatures, and the Cu/G catalyst at 800 °C exhibits the highest ORR activity (Fig. S7a). As shown in Fig. 5a, the onset potential, half-wave potential and diffusion-limited current density of ORR on the optimized Cu/G are comparable to those on benchmark Pt/C, and significantly higher than pristine graphene (p-G) as well as N-doped graphene (N-G). The exact half-wave potential and kinetic current density calculated using Koutecky-Levich plots [35] (Fig. S8) are summarized in Fig. 5b. The Cu/G exhibits even more positive half-wave potential and higher kinetic current density at 0.85 V (0.847 V and 3.787 mA $cm_{disk}^{-2}$) than Pt/C (0.837 V and 3.104 mA $cm_{disk}^{-2}$) at the comparable metal loadings (Pt/C: 20 $\mu g_{Pt}$ $cm^{-2}$ *v.s.* Cu/G: 21.6 $\mu g_{Cu}$ $cm^{-2}$). Moreover, the Tafel slope for Cu/G (36 mV $dec^{-1}$) is smaller than that for Pt/C (70.7 mV $dec^{-1}$), indicating more favored ORR kinetics on Cu/G as the overpotential increases, as shown in Fig. S7b [72]. The superior ORR activity of Cu/G should be attributed to the highly-loaded Cu single atoms, whose electronic properties regulate the adsorption behavior of intermediates during ORR [73–75].

DFT calculation is performed to explain the superior ORR performance of Cu/G. To reference the ORR activity of single Cu atoms, Cu (111) surface is also taken into account. The calculated free energy diagrams of ORR based on four-electron pathway [76] on Cu/G and Cu (111) are shown in Fig. 5c. With 0.94 V overpotential applied, all the elementary steps on Cu/G become exothermic and the reduction of oxygen molecules becomes spontaneous [77]. In contrast, an additional overpotential of 175 mV is still necessary for the desorption of OH* on Cu(111) due to the overstrong adsorption of intermediates as indicated by the much more negative free energy. The result suggests that single Cu atoms dispersed on graphene should exhibit higher ORR activity

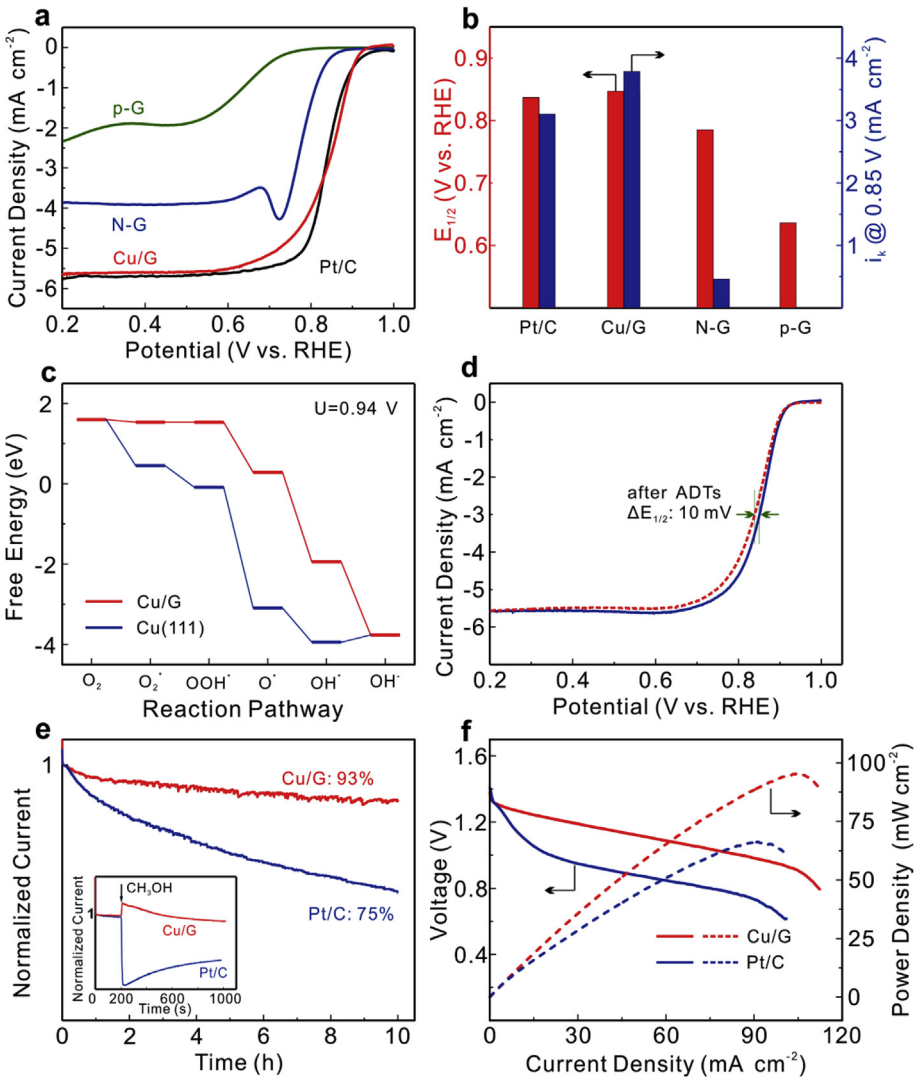


**Fig. 5. The performance of Cu/G as ORR catalyst.** (a) ORR polarization curves at 1600 rpm measured in $O_2$ saturated 0.1 mol $L^{-1}$ KOH; (b) half-wave potential and kinetic current density at 0.85 V of Pt/C, Cu/G, N-G and p-G; (c) free energy diagrams of Cu/G and Cu(111) with 0.94 V overpotential applied; (d) ORR polarization curves of Cu/G before and after ADTs; (e) 10-h normalized chronoamperometric curves of Cu/G and Pt/C at 0.65 V and (inset) normalized chronoamperometric curves with 5 mL methanol added at 200 s; (f) polarization curves (solid lines) and power density curves (dashed lines) of Zn-air batteries assembled using Cu/G and 20 wt% Pt/C as cathode catalysts.

than bulk Cu metal, highlighting the value of atomization of Cu for enhanced ORR catalysis.

Rotating ring disk electrode (RRDE) test is also performed to look into the details of the ORR mechanism. From the ORR and the hydrogen peroxide oxidation currents recorded respectively on the disk and ring electrodes (Fig. S9a), the electron transfer number is calculated to be 3.96 on Cu/G at 0.8 V (Fig. S9b), revealing a major four-electron ORR mechanism. Our Cu/G with high loading level is one of the most efficient ORR catalysts in terms of TOF (0.116 e $site^{-1}$ $s^{-1}$ @ 0.85 V) as well as half-wave potential (Table S2), demonstrating that rational design of high-density single-atom active sites alternative to Fe and Co can also achieve rather high ORR activity.

The long-term stability of Cu/G is evaluated using accelerated durability test (ADT) and chronoamperometry. After 10000 cycles of ADTs between 0.6 V and 1.0 V in $O_2$-saturated 0.1 mol $L^{-1}$ KOH, the ORR polarization curve of Cu/G shows only 10 mV decline in half-wave potential (Fig. 5d), much smaller than Pt/C (22 mV decline as shown in Fig. S10). By setting the electrode potential at 0.65 V, the ORR current loss after 10 h of chronoamperometric test is < 7% for Cu/G, while > 25% for Pt/C (Fig. 5e). These results reveal the significantly better long-term durability of Cu/G than Pt/C. Further, as shown in the inset of Fig. 5e, unlike Pt/C [78], Cu/G shows an excellent tolerance towards methanol during the chronoamperometric test, which is of significance to catalyzing the oxygen reduction in some direct-type fuel cells.

The practical applicability of our Cu/G is evaluated in alkaline zinc-air batteries. As demonstrated by polarization and power density curves in Fig. 5f, the Cu/G based battery apparently outperforms the Pt/C-based one even at the same catalyst loading of 0.4 mg $cm^{-2}$. It delivers a peak power density of 95.3 mW $cm^{-2}$, 1.44 time as high as Pt/C (66.25 mW $cm^{-2}$). This outstanding performance should be endowed by the highly-dispersed Cu atoms, as well as the high electronic conductivity and facile mass transport from the three-dimensional graphene structure. Two Cu/G-based batteries in series can readily power a red light-emitting diode (1.8 V) as illustrated in Fig. S11, further confirming the advantageous ORR performance of Cu/G in a real battery system.

## 4. Conclusion

A unique confined self-initiated dispersing protocol is demonstrated for the first time to be an effective method to fabricate high loading single-atom Cu dispersed on graphene (Cu/G). This innovative in-situ dispersing protocol generates highly active gaseous Cu-containing intermediates, which can essentially circumvent the massive agglomeration of metal atoms in the conventional procedures, and facilitate the dispersing of Cu on graphene. Consequently, the highest loading level (5.4 wt%) of single-atom Cu dispersed on graphene matrix is achieved. The resultant Cu/G with high loading level presents remarkable activity towards oxygen reduction reaction, which even outperforms the commercial Pt/C catalyst. Our work provides a new efficient strategy for the

fabrication of single-atom metals dispersed on graphene materials with high loading levels. Meanwhile, our findings broaden the choice of non-noble metal ORR catalysts and bring new insights into design of high-density single-atom active sites in electrocatalysis.

## Acknowledgements

This work was financially supported by the National Natural Science Foundation of China (Grant No. 21433003) and (Grant No. 21376057). Research at the University of Western Ontario was supported by Natural Sciences and Engineering Research Council of Canada (NSERC), Canada Foundation for Innovation (CFI), and Canada Research Chair (CRC) of Canada. The Canadian Light Source is supported by Natural Sciences and Engineering Research Council of Canada (NSERC), National Research Council of Canada (NRC), Canadian Institutes of Health Research (CIHR) and the University of Saskatchewan.

## Appendix A. Supplementary data

Supplementary data to this article can be found online at https://doi.org/10.1016/j.nanoen.2019.104088.

## References

[1] L. Zhang, K. Doyle-Davis, X. Sun, Energy Environ. Sci. 12 (2019) 492–517.
[2] C. Zhu, S. Fu, Q. Shi, D. Du, Y. Lin, Angew. Chem. Int. Ed. 56 (2017) 13944–13960.
[3] X.F. Yang, A. Wang, B. Qiao, J. Li, J. Liu, T. Zhang, Acc. Chem. Res. 46 (2013) 1740–1748.
[4] P. Zhai, T. Wang, W. Yang, S. Cui, P. Zhang, A. Nie, Q. Zhang, Y. Gong, Adv. Energy Mater. 9 (2019) 1804019.
[5] S. Ji, Y. Chen, S. Zhao, W. Chen, L. Shi, Y. Wang, J. Dong, Z. Li, F. Li, C. Chen, Q. Peng, J. Li, D. Wang, Y. Li, Angew. Chem. Int. Ed. 58 (2019) 4271–4275.
[6] Z. Du, X. Chen, W. Hu, C. Chuang, S. Xie, A. Hu, W. Yan, X. Kong, X. Wu, H. Ji, L. Wan, J. Am. Chem. Soc. 141 (2019) 3977–3985.
[7] X. Li, X. Huang, S. Xi, S. Miao, J. Ding, W. Cai, S. Liu, X. Yang, H. Yang, J. Gao, J. Wang, Y. Huang, T. Zhang, B. Liu, J. Am. Chem. Soc. 140 (2018) 12469–12475.
[8] Y. Ye, F. Cai, H. Li, H. Wu, G. Wang, Y. Li, S. Miao, S. Xie, R. Si, J. Wang, X. Bao, Nano Energy 38 (2017) 281–289.
[9] J. Xie, J.D. Kammert, N. Kaylor, J.W. Zheng, E. Choi, H.N. Pham, X. Sang, E. Stavitski, K. Attenkofer, R.R. Unocic, A.K. Datye, R.J. Davis, ACS Catal. 8 (2018) 3875–3884.
[10] Y. Zhu, T. Cao, C. Cao, J. Luo, W. Chen, L. Zheng, J. Dong, J. Zhang, Y. Han, Z. Li, C. Chen, Q. Peng, D. Wang, Y. Li, ACS Catal. 8 (2018) 10004–10011.
[11] W. Liu, L. Zhang, W. Yan, X. Liu, X. Yang, S. Miao, W. Wang, A. Wang, T. Zhang, Chem. Sci. 7 (2016) 5758–5764.
[12] M. Zhang, Y.G. Wang, W. Chen, J. Dong, L. Zheng, J. Luo, J. Wan, S. Tian, W.C. Cheong, D. Wang, Y. Li, J. Am. Chem. Soc. 139 (2017) 10976–10979.
[13] Y. Zhu, W. Sun, W. Chen, T. Cao, Y. Xiong, J. Luo, J. Dong, L. Zheng, J. Zhang, X. Wang, C. Chen, Q. Peng, D. Wang, Y. Li, Adv. Funct. Mater. 28 (2018) 1802167.
[14] C. Lei, H. Chen, J. Cao, J. Yang, M. Qiu, Y. Xia, C. Yuan, B. Yang, Z. Li, X. Zhang, L. Lei, J. Abbott, Y. Zhong, X. Xia, G. Wu, Q. He, Y. Hou, Adv. Energy Mater. 8 (2018) 1801912.
[15] Y. Cheng, S. Zhao, B. Johannessen, J.-P. Veder, M. Saunders, M.R. Rowles, M. Cheng, C. Liu, M.F. Chisholm, R. De Marco, H.-M. Cheng, S.-Z. Yang, S.P. Jiang, Adv. Mater. 30 (2018) 1706287.
[16] Z. Geng, Y. Liu, X. Kong, P. Li, K. Li, Z. Liu, J. Du, M. Shu, R. Si, J. Zeng, Adv. Mater. 30 (2018) 1803498.
[17] C. Gao, S. Chen, Y. Wang, J. Wang, X. Zheng, J. Zhu, L. Song, W. Zhang, Y. Xiong, Adv. Mater. 30 (2018) 1704624.
[18] J. Zhang, G. Chen, K. Müllen, X. Feng, Adv. Mater. 30 (2018) 1800528.
[19] X. Huang, X. Qi, F. Boey, H. Zhang, Chem. Soc. Rev. 41 (2012) 666–686.
[20] P. Tang, G. Hu, M. Li, D. Ma, ACS Catal. 6 (2016) 6948–6958.
[21] H. Yan, X. Zhao, N. Guo, Z. Lyu, Y. Du, S. Xi, R. Guo, C. Chen, Z. Chen, W. Liu, C. Yao, J. Li, S.J. Pennycook, W. Chen, C. Su, C. Zhang, J. Lu, Nat. Commun. 9 (2018) 3197.
[22] M. Li, S. Wu, X. Yang, J. Hu, L. Peng, L. Bai, Q. Huo, J. Guan, Appl. Catal. A Gen. 543 (2017) 61–66.
[23] X. Gao, Y. Zhu, D. Yi, J. Zhou, S. Zhang, C. Yin, F. Ding, S. Zhang, X. Yi, J. Wang, L. Tong, Y. Han, Z. Liu, J. Zhang, Sci. Adv. 4 (2018) 6378.
[24] K. Jiang, S. Siahrostami, T. Zheng, Y. Hu, S. Hwang, E. Stavitski, Y. Peng, J. Dynes, M. Gangisetty, D. Su, K. Attenkofer, H. Wang, Energy Environ. Sci. 11 (2018) 893–903.
[25] N. Cheng, S. Stambula, D. Wang, M.N. Banis, J. Liu, A. Riese, B. Xiao, R. Li, T.-K. Sham, L.-M. Liu, G.A. Botton, X. Sun, Nat. Commun. 7 (2016) 13638.
[26] H. Fei, J. Dong, C. Wan, Z. Zhao, X. Xu, Z. Lin, Y. Wang, H. Liu, K. Zang, J. Luo, S. Zhao, W. Hu, W. Yan, I. Shakir, Y. Huang, X. Duan, Adv. Mater. 30 (2018) 1802146.
[27] H. Fei, J. Dong, M.J. Arellano-Jiménez, G. Ye, N. Dong Kim, E.L.G. Samuel, Z. Peng, Z. Zhu, F. Qin, J. Bao, M.J. Yacaman, P.M. Ajayan, D. Chen, J.M. Tour, Nat. Commun. 6 (2015) 8668.
[28] M.D. Hossain, Z. Liu, M. Zhuang, X. Yan, G.-L. Xu, C.A. Gadre, A. Tyagi, I.H. Abidi, C.-J. Sun, H. Wong, A. Guda, Y. Hao, X. Pan, K. Amine, Z. Luo, Adv. Energy Mater. 9 (2019) 1803689.
[29] Y. Qu, B. Chen, Z. Li, X. Duan, L. Wang, Y. Lin, T. Yuan, F. Zhou, Y. Hu, Z. Yang, C. Zhao, J. Wang, C. Zhao, Y. Hu, G. Wu, Q. Zhang, Q. Xu, B. Liu, P. Gao, R. You, W. Huang, L. Zheng, L. Gu, Y. Wu, Y. Li, J. Am. Chem. Soc. 141 (2019) 4505–4509.
[30] S. Ye, F. Luo, Q. Zhang, P. Zhang, T. Xu, Q. Wang, D. He, L. Guo, Y. Zhang, C. He, X. Ouyang, M. Gu, J. Liu, X. Sun, Energy Environ. Sci. 12 (2019) 1000–1007.
[31] Y. Shi, C. Zhao, H. Wei, J. Guo, S. Liang, A. Wang, T. Zhang, J. Liu, T. Ma, Adv. Mater. 26 (2014) 8147–8153.
[32] X. Li, W. Bi, M. Chen, Y. Sun, H. Ju, W. Yan, J. Zhu, X. Wu, W. Chu, C. Wu, Y. Xie, J. Am. Chem. Soc. 139 (2017) 14889–14892.
[33] H. Itoi, H. Nishihara, S. Kobayashi, S. Ittisanronnachai, T. Ishii, R. Berenguer, M. Ito, D. Matsumura, T. Kyotani, J. Phys. Chem. C 121 (2017) 7892–7902.
[34] Y. Sun, C. Du, G. Han, Y. Qu, L. Du, Y. Wang, G. Chen, Y. Gao, G. Yin, Electrochim. Acta 212 (2016) 313–321.
[35] B. You, N. Jiang, M. Sheng, W.S. Drisdell, J. Yano, Y. Sun, ACS Catal. 5 (2015) 7068–7076.
[36] D. Malko, A. Kucernak, T. Lopes, Nat. Commun. 7 (2016) 13285.
[37] L.T. Song, Z.Y. Wu, F. Zhou, H.W. Liang, Z.Y. Yu, S.H. Yu, Small 12 (2016) 6398–6406.
[38] J. VandeVondele, M. Krack, F. Mohamed, M. Parrinello, T. Chassaing, J. Hutter, Comput. Phys. Commun. 167 (2005) 103–128.
[39] S. Grimme, J. Antony, S. Ehrlich, H. Krieg, J. Chem. Phys. 132 (2010) 154104.
[40] S. Goedecker, M. Teter, J. Hutter, Phys. Rev. B. 54 (1996) 1703–1710.
[41] C. Hartwigsen, S. Goedecker, J. Hutter, Phys. Rev. B. 58 (1998) 3641–3662.
[42] A. Seifitokaldani, C.M. Gabardo, T. Burdyny, C. Dinh, J.P. Edwards, M.G. Kibria, O.S. Bushuyev, S.O. Kelley, D. Sinton, E.H. Sargent, J. Am. Chem. Soc. 140 (2018) 3833–3837.
[43] P. Atkins, J. De Paula, J. Keeler, Atkins' Physical Chemistry, Oxford university press, 2018.
[44] S. Wang, D. Yu, L. Dai, D. Chang, J. Baek, ACS Nano 5 (2011) 6202–6209.
[45] Z. Luo, C. Tan, X. Zhang, J. Chen, X. Cao, B. Li, Y. Zong, L. Huang, X. Huang, L. Wang, W. Huang, H. Zhang, Small 12 (2016) 5920–5926.
[46] S. Zhang, L. Sui, H. Kang, H. Dong, L. Dong, L. Yu, Small 14 (2018) 1702570.
[47] C. Cheng, S. Li, Y. Xia, L. Ma, C. Nie, C. Roth, A. Thomas, R. Haag, Adv. Mater. 30 (2018) 1802669.
[48] M. Xiao, J. Zhu, L. Ma, Z. Jin, J. Ge, X. Deng, Y. Hou, Q. He, J. Li, Q. Jia, S. Mukerjee, R. Yang, Z. Jiang, D. Su, C. Liu, W. Xing, ACS Catal. 8 (2018) 2824–2832.
[49] J. Wang, G. Han, L. Wang, L. Du, G. Chen, Y. Gao, Y. Ma, C. Du, X. Cheng, P. Zuo, G. Yin, Small 14 (2018) 1704282.
[50] J. Jia, W. Zhou, Z. Wei, T. Xiong, G. Li, L. Zhao, X. Zhang, H. Liu, J. Zhou, S. Chen, Nano Energy 41 (2017) 749–757.
[51] J. Guo, Y. Li, Y. Cheng, L. Dai, Z. Xiang, ACS Nano 11 (2017) 8379–8386.
[52] W. Wei, Y. Lu, W. Chen, S. Chen, J. Am. Chem. Soc. 133 (2011) 2060–2063.
[53] J. Wang, K. Wang, F.-B. Wang, X.-H. Xia, Nat. Commun. 5 (2014) 5285.
[54] H. Wu, H. Li, X. Zhao, Q. Liu, J. Wang, J. Xiao, S. Xie, R. Si, F. Yang, S. Miao, X. Guo, G. Wang, X. Bao, Energy Environ. Sci. 9 (2016) 3736–3745.
[55] Y. Chen, S. Ji, Y. Wang, J. Dong, W. Chen, Z. Li, R. Shen, L. Zheng, Z. Zhuang, D. Wang, Y. Li, Angew. Chem. Int. Ed. 56 (2017) 6937–6941.
[56] X. Li, J. Yu, J. Jia, A. Wang, L. Zhao, T. Xiong, H. Liu, W. Zhou, Nano Energy 62 (2019) 127–135.
[57] Y. Zheng, Y. Jiao, Y. Zhu, Q. Cai, A. Vasileff, L.H. Li, Y. Han, Y. Chen, S.-Z. Qiao, J. Am. Chem. Soc. 139 (2017) 3336–3339.
[58] J. Wang, Z. Huang, W. Liu, C.-R. Chang, H. Tang, Z. Li, W. Chen, C. Jia, T. Yao, S. Wei, Y. Wu, Y. Li, J. Am. Chem. Soc. 139 (2017) 17281–17284.
[59] J.J. Rehr, R.C. Albers, Rev. Mod. Phys. 72 (2000) 621–654.
[60] A.A. Gewirth, J.A. Varnell, A.M. DiAscro, Chem. Rev. 118 (2018) 2313–2339.
[61] Y. Qiu, L. Xin, F. Jia, J. Xie, W. Li, Langmuir 32 (2016) 12569–12578.
[62] H. Yu, L. Shang, T. Bian, R. Shi, G.I.N. Waterhouse, Y. Zhao, C. Zhou, L.-Z. Wu, C.-H. Tung, T. Zhang, Adv. Mater. 28 (2016) 5080–5086.
[63] M.-Q. Wang, W. Yang, H. Wang, C. Chen, Z. Zhou, S. Sun, ACS Catal. 4 (2014) 3928–3936.
[64] S. Qiao, R.W. Mitchell, B. Coulson, D.V. Jowett, B.R.G. Johnson, R. Brydson, M. Isaacs, A.F. Lee, R.E. Douthwaite, Carbon N. Y. 106 (2016) 320–329.
[65] F. Goettmann, A. Fischer, M. Antonietti, A. Thomas, Angew. Chem. Int. Ed. 45 (2006) 4467–4471.
[66] Y. Zhao, J. Liang, C. Wang, J. Ma, G.G. Wallace, Adv. Energy Mater. 8 (2018) 1702524.
[67] Y. Guo, P. Yuan, J. Zhang, Y. Hu, I.S. Amiinu, X. Wang, J. Zhou, H. Xia, Z. Song, Q. Xu, S. Mu, ACS Nano 12 (2018) 1894–1901.
[68] K. Strickland, E. Miner, Q. Jia, U. Tylus, N. Ramaswamy, W. Liang, M.-T. Sougrati, F. Jaouen, S. Mukerjee, Nat. Commun. 6 (2015) 7343.
[69] Y. He, S. Hwang, D.A. Cullen, M.A. Uddin, L. Langhorst, B. Li, S. Karakalos, A.J. Kropf, E.C. Wegener, J. Sokolowski, M. Chen, D. Myers, D. Su, K.L. More, G. Wang, S. Litster, G. Wu, Energy Environ. Sci. 12 (2019) 250–260.
[70] Z. Zhang, J. Sun, F. Wang, L. Dai, Angew. Chem. Int. Ed. 57 (2018) 9038–9043.
[71] C. Zhang, J.M. Tour, Nat. Catal. 1 (2018) 900–902.
[72] Z. Jiang, Z.-J. Jiang, T. Maiyalagan, A. Manthiram, J. Mater. Chem. A 4 (2016) 5877–5889.
[73] H. Zhang, W. Zhou, T. Chen, B.Y. Guan, Z. Li, X.W.D. Lou, Energy Environ. Sci. 11 (2018) 1980–1984.
[74] H.J. Qiu, Y. Ito, W. Cong, Y. Tan, P. Liu, A. Hirata, T. Fujita, Z. Tang, M. Chen,

Angew. Chem. Int. Ed. 54 (2015) 14031–14035.
[75] Y. Han, Y. Wang, R. Xu, W. Chen, L. Zheng, A. Han, Y. Zhu, J. Zhang, H. Zhang, J. Luo, C. Chen, Q. Peng, D. Wang, Y. Li, Energy Environ. Sci. 11 (2018) 2348–2352.
[76] R. Jiang, L. Li, T. Sheng, G. Hu, Y. Chen, L. Wang, J. Am. Chem. Soc. 140 (2018) 11594–11598.
[77] D. Ji, L. Fan, L. Li, S. Peng, D. Yu, J. Song, S. Ramakrishna, S. Guo, Adv. Mater. 31 (2019) 1808267.
[78] L. Yang, J. Yu, Z. Wei, G. Li, L. Cao, W. Zhuo, S. Chen, Nano Energy 41 (2017) 772–779.